Chemistry Europe
European Chemical Societies Publishing
Batteries & Supercaps

RESEARCH ARTICLE OPEN ACCESS

Room Temperature Fabrication of Binder-Free $Na_3V_2(PO_4)_3$/C High-Loading Electrode Films via the Powder Aerosol Deposition Method

Mutlucan Sozak[1,2] | Sofie Knies[2,3] | Matteo Bianchini[2,3] | Ralf Moos[1,2]

[1]Department of Functional Materials, University of Bayreuth, Bayreuth, Germany | [2]Bavarian Center for Battery Technology (BayBatt), University of Bayreuth, Bayreuth, Germany | [3]Chair of Inorganic Active Materials for Electrochemical Energy Storage, University of Bayreuth, Bayreuth, Germany

Correspondence: Mutlucan Sozak (Mutlucan.Sozak@uni-bayreuth.de) | Ralf Moos (functional.materials@uni-bayreuth.de)

Received: 14 November 2025 | **Revised:** 13 December 2025 | **Accepted:** 28 December 2025

Keywords: cathodes | ceramics | energy storage | Na-ion transportation | $Na_3V_2(PO_4)_3$ | NaSICON | polyanions | powder aerosol deposition | sodium-ion batteries

ABSTRACT

The powder aerosol deposition (PAD or aerosol deposition method [ADM]) and tape casting were used to manufacture $Na_3V_2(PO_4)_3$/C (NVP/C) electrodes from the same synthesized powder batch. We demonstrate that Na-based, binder-free and solvent-free thick PAD electrodes can be directly deposited onto aluminum current collectors. Tape-cast electrodes were fabricated on aluminum foil to serve as a reference for electrochemical benchmarking. Galvanostatic cycling was performed at a C-rate of C/10 between 1.5–4.5 and 2–4 V versus Na^+/Na using a liquid electrolyte in coin cells. PAD electrodes with varying cathode active material (CAM) loadings were produced to evaluate the effect of loading and posttreatment on the electrochemical performance. While tape-cast electrodes show consistent capacities (~90 mAh g^{-1} at C/10), PAD electrodes delivered significantly lower specific capacities depending on CAM loading and posttreatment. By correlating delivered charge with active mass and thickness, we show that the charge extracted from PAD-NVP/C cathode exhibit a plateau at ~0.15–0.18 mAh, independent of CAM loading. This indicates that only a thin fraction of surface region participates in de/-intercalation. These findings reveal the utilization limits in thick PAD cathodes and provide insight toward enabling their future industrialization.

1 | Introduction

Intensive research into sodium (Na)-based batteries suggests that these devices are strong candidates for energy storage solutions not only for stationary applications but also for mid-range electromobility [1].

The driving force behind Na-ion battery research is the widespread availability of sodium resources and the analogous chemistry of Na-ion batteries to their lithium (Li) counterparts. According to the Al-Na phase diagram [2], sodium does not alloy with aluminum. Therefore, Na-ion battery design allows the replacement of Al as the current collector (CC) on the anode and cathode side instead of copper. Being more affordable and lighter, aluminum as CC results in weight and cost savings.

The 3D framework of $Na_3V_2(PO_4)_3$ (NVP) was first investigated in 2002 by Uebou et al. [3]. Its rhombohedral NaSICON structure enables to insert and extract sodium ions, and it is considered to be one of the most promising cathode candidates for Na-ion batteries due to its high theoretical capacity (117 mAh g^{-1}). Since then, considerable effort has been devoted to enhancing the cycling stability of this material and to exploiting its maximum capacity. Recent studies have shown that advanced particle engineering, nanoscale carbon coatings, and interface design can significantly enhance the performance of NVP/C

electrodes under practical liquid-electrolyte conditions [4–6]. One strategy to achieve this is to synthesize NVP/C composite cathode powders with conductive carbon coating [7–10]. Other strategies manipulate the microstructure of the NVP/C powder by altering the synthesis parameters [11], or use doping elements to replace the vanadium with the elements such as Fe^{2+} [12], Mn^{2+} [13], Ti^{3+} [14] and K^{+} [15], or fluorinate the compound, resulting however in a different crystal structure ($Na_3V_2(PO_4)_2F_3$, NVPF) [16]. The NVP has two active redox couples; V^{4+}/V^{3+} at 3.4 V and V^{3+}/V^{2+} at 1.6 V vs Na^{+}/Na. Therefore, it can be used for both the positive and negative electrodes, including to build symmetric cells with both liquid and solid electrolytes (SEs) [17, 18].

The PAD method is a room-temperature dry powder spray technique for fabricating fully dense nanocrystalline functional ceramic films of varying thickness on various substrate materials, such as metals, glasses, and polymers. It is also known as ADM [19]. The method was initially developed by Akedo et al. [20]. Akedo's group revealed the fundamental principles including the deposition mechanisms.

The PAD process has been investigated to manufacture key components for lithium batteries and solid-state battery (SSB) architectures, including SEs, such as LLZO [21, 22], LATP [23] and LAGP [24, 25], and cathode active materials (CAMs), such as LFP [26], LTO [27], LCO [28] and NMC [29–32]. For Na-based components, so far there have been fewer reports. Some of the few examples include the application as SE, e.g., NZSP [33], NZTO [34], and as CAM, NVP [35, 36].

The PAD process is particularly interesting for electrode manufacturing, as it does not require any type of binder or solvent constituent to ensure the integrity of the electrode. This means that no inactive components are included in the electrode composition. In addition, process steps, such as solvent evaporation are eliminated, resulting in a simplified electrode manufacturing process. Moreover, the process is conducted at room temperature to produce functional ceramic layers in a relatively short time.

NVP powder was firstly powder aerosol deposited on stainless steel by Sam Oh et al. [35]. It was reported that electrodes with active mass loading of 0.26–0.39 mg cm^{-2} deliver a reversible areal capacity of 32.2 µAh cm^{-2} at a current density of 96.4 µAcm^{-2} against sodium metal. Wang et al. [36] reported the aerosol deposition of NVP powders on 1 mm thick $Na_3Zr_2Si_2PO_{12}$ (NZSP) solid electrolyte pellets. The Na-based quasi SSB (with liquid electrolyte addition) with a CAM loading of 0.2 mg cm^{-2} yielded 94 mAh g^{-1} discharge capacity against Na^{+}/Na. In both cases, the electrode loading as well as the applied currents were very low.

In this work, we aim to elucidate the cycling performance of powder aerosol deposited sodium-based NVP/C composite electrodes on aluminum substrates with a high CAM loading, close to the typical values used in tape-cast electrodes for Na-ion cells. We then compare the performance of these electrodes with those fabricated by tape casting, which is the most common industrial electrode fabrication method. We evaluate the influence of CAM loading in dense PAD NVP/C cathode layers on the cycling performance, and we identify the microstructural limitations that restrict active material utilization in PAD electrodes.

2 | Experimental Section

2.1 | Synthesis of NVP/C Composite Cathodes

The synthesis of $Na_3V_2(PO_4)_3$/C composites was carried out by a solid-state route with an intermediate calcination step. The raw materials of Na_2CO_3 (≥99.9%, Sigma Aldrich), $NH_4H_2PO_4$ (≥99.5%, Sigma Aldrich), V_2O_5 (≥99.6%, Sigma Aldrich), and citric acid (≥99.5%, Sigma Aldrich) were weighed and mixed in a planetary ball mill using yttria-stabilized ZrO_2 milling media. Citric acid was chosen as the carbon source and reducing agent. It was included in the mixture with 30 wt.% (with respect to the expected weight of the final product). The starting materials were homogenized in cyclohexane medium for 15 min at 400 rpm. The homogenized mixture was transferred to a crystallization dish and left to evaporate the cyclohexane under a fume hood. For the dried mixture, the first calcination step was carried out at 300°C in a muffle type furnace (Nabertherm LT 08/16) under ambient atmosphere. The intermediate product was crushed in a mortar and pressed into pellets (Ø20 mm, 5 g each). The pellets were placed in cylindrical alumina crucible and calcined in a tube furnace (Carbolite Gero, STF 15/450, Neuhausen, Germany) in an Ar/H_2 (95/5%) atmosphere at 750°C for 20 h. The calcined pellets were crushed in a mortar and then ball-milled with the parameters given in the next section to obtain a suitable particle size distribution (PSD) for the PAD process.

2.2 | NVP/C Cathode Layers via PAD

Carbon-coated sodium vanadium phosphate (NVP/C) composite films were fabricated using a custom-built PAD device. The setup in our laboratory and its fundamentals have been reported for instance in [37]. The powders were ground in a planetary ball mill (Pulverisette 5, Fritsch GmbH, Germany) using zirconia grinding media at a speed of 300 rpm for 2 h in cyclohexane. The milling medium was then evaporated using a rotary evaporator (Heidolph Hei-VAP Advantage, Germany). The powder was sieved through 90 µm mesh sieve and stored in a drying oven at 200°C overnight. The powders were then sprayed onto aluminum substrates (Ø10 mm, ~300 µm thickness). The substrates were manually polished on one side using FEPA P #500, #800, #1200, #2000, and #4000 abrasive papers for 2 min in each step (see Figure S1). The other side of the substrates was grinded only with #800 grit paper for 2 min to remove the oxide layer.

The deposition parameters that were varied to obtain different CAM loadings on the Al substrates are listed in Table 1. Two different sets of deposition processes were performed. The following parameters were kept constant; oxygen gas was supplied to the aerosol flask, the distance between the nozzle (10 mm by 0.5 mm, slit orifice) and the substrates were

TABLE 1 | Deposition parameters to obtain different CAM mass on the Al substrates.

Spraying parameters - Samples	PAD – 1st set	PAD – 2nd set
Scans	25	12
Gas flow	8 l min^{-1}	5 l min^{-1}

adjusted to 3 mm, and the sample holder stage was moved horizontally at a speed of 1 mm s^{-1} to deposit NVP/C films. CAM loading on the powder aerosol deposited substrates was determined by weighing the substrates before and after deposition.

2.3 | NVP/C Cathode Layers via Tape Casting

NVP/C tape-cast films were prepared using polyvinylidene fluoride (PVdF) as a binder (Solef5130 7.5 wt.%), 1-Methyl-2-pyrrolidone as a solvent (NMP, 99.5%, Sigma Aldrich), carbon black (99+ %, ThermoFisher Scientific), and CAM (NVP/C, sieved through 56 µm mesh). The above-mentioned milling parameters apply to the powder used for tape casting. The weight ratio of CAM:carbon:binder was 80:10:10. The preparation of the slurry was as follows; (i) NMP solution containing 7.5 wt.% of PVDF binder was weighed in a plastic container, (ii) carbon black was added, (iii) additional solvent was included utilizing a syringe, and (iv) the constituents were mixed with a planetary centrifugal mixer (Thinky ARE-250, Japan) at 2000 rpm for 2 min, followed by 400 rpm for 2 min for degassing. The rest of the solvent was added stepwise, followed by mixing at each step until a consistent slurry without agglomerates was obtained. The slurry was transferred to the doctor blade (120 µm opening) and cast onto aluminum foil (15 µm thick) at a speed of 1 mm s^{-1}. The castings were then placed in a drying oven and kept overnight at 100°C under vacuum (20 mbar). Electrodes with a diameter of 13 mm were punched out and stored in the glovebox after being kept in the antechamber at 100°C for 8 h.

2.4 | Electrochemical Measurements

The performance of powder aerosol deposited and of tape-cast cathodes was evaluated in CR2032 coin cells (Hohsen Corp., Japan), which were assembled in an argon-filled glovebox. An exploded view of a coin cell is shown in Figure 1. The coin cells were assembled using 1 M $NaPF_6$ EC:EMC 30:70 wt.% (Elyte GmbH) and Na metal (Sigma Aldrich, 99.9%) were utilized as the electrolyte and anode, respectively. A separator (Ø17 mm, Whatman GF/A) was used in between the electrodes. The sodium metal was rolled to a thickness of 0.6 mm. Round shaped anodes of 14 mm and 12 mm were punched for the tape-cast and powder aerosol deposited electrodes, respectively. The coin cells were crimped using a pressure-controlled cell crimper at 0.8 tons (MTI Corp., USA) along with the disk spacers (1 mm thick, Ø15.4 mm) and wave washers (1.4 mm height, Ø15 mm) inside. The open circuit voltage of the assembled cells was ~2.8 V (vs. Na^+/Na).

In the standard cycling procedure, the cells were cycled at a C-rate of 0.1C (calculated according to the theoretical capacity of $Na_3V_2(PO_4)_3$–117 mAh g^{-1}) for 20 cycles in the range of 1.5–4.5 V or 2–4 V. The rate capacity performances were determined in the same potential range at C-rates of 0.1C, 0.2C, 0.5C, 1C, 2C, 5C and 10C for 5 cycles in each step. The carbon content of the CAM was excluded for the calculation of CAM loading to determine specific charge/discharge capacities of the cathodes.

2.5 | Materials Characterization

Prior to the deposition process, the particle size of the powders was measured by laser scattering (Mastersizer 2000, Malvern Instruments Ltd, Malvern, UK). Powders were mixed with a dispenser, and the mixtures were placed in an ultrasonic bath for 30 s to achieve homogeneous distribution prior to measurement.

Phase compositions of powders and films were determined by X-ray diffraction analysis (XRD, D8 Advance, Bruker, diffractometer with Ge-$K_{\alpha 1}$ monochromator –1.5406 Å and energy-dispersive 1-D LYNXEYE detector). The powders were exposed to X-rays between 10° and 80° (2θ) in 0.02 steps for 0.2 s hold time and the XRD parameters on the films were determined as 10°–80° in steps of 0.01° for 0.5 s exposure time. Rietveld analyses were carried out using Profex (5.5.2) software [38]. Details regarding to Rietveld analysis carried out for this study can be found in the Supporting Information.

The carbon content of the powder was determined by thermogravimetric analysis combined with mass spectrometry (TG-MS) using a Netzsch STA 449F5 instrument (Selb, Germany) with Pt-Rh20% crucibles. The analysis was carried out in synthetic air at a heating rate of 10 K min^{-1} to 700°C.

The microstructure of sprayed films was examined by scanning electron microscopy (SEM, FEI Quanta FEG 250, ThermoFisher Scientific, USA) from cross-sections. To prepare samples for SEM, they were first embedded in resin and then cut in half. The surfaces were then grinded and polished.

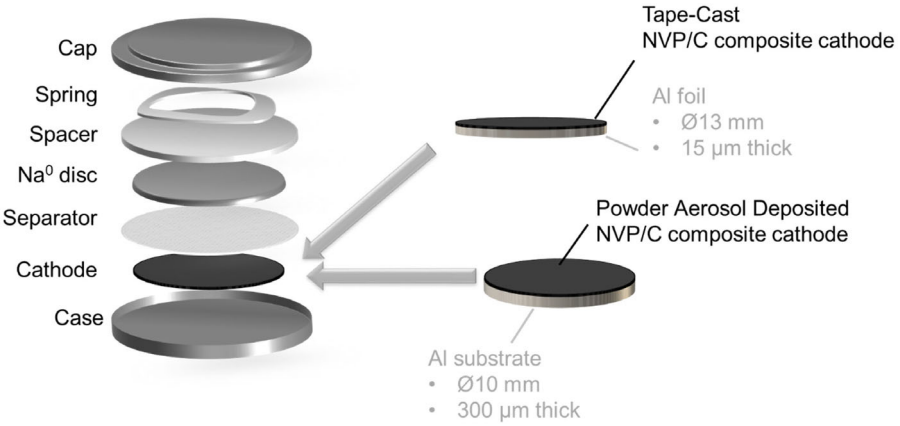

FIGURE 1 | Exploded-view of CR2032 coin cell. Two different positive electrode configurations were used; tape-cast NVP/C on Al foil (15 µm) and powder aerosol deposited NVP/C on Al substrates (~300 µm).

3 | Results and Discussion

3.1 | Characterization of NVP/C Powder

An X-ray diffraction pattern of a synthesized NVP/C powder is shown in Figure 2a. It shows that the positions and the relative intensities of the reflections agree with the simulated pattern of $Na_3V_2(PO_4)_3$ from the PDF-4+ database (04-016-8358). The synthesized NVP/C powder exhibits a rhombohedral crystal structure belonging to the $R\bar{3}c$ space group. The sharp reflections with strong intensity indicate a highly crystalline powder. The unmarked reflections belong to a superstructure phase that can be attributed to monoclinic distortions at room temperature [18].

The carbon content of the NVP/C composite powder was determined by TG-MS analysis. In Figure 2b, the difference in weight loss between 300°C and 450°C was considered as the carbon content; therefore, CO_2 detection by mass spectroscopy below 450°C was attributed to carbon species. It was determined to be ~2.2 wt.%, since carbon burns in synthetic air in this temperature range. The increase in NVP mass above 450°C is due to the oxidation of V^{3+} to V^{5+} [39].

Some properties of the starting powders, such as the PSD, have an enormous influence on the deposition behavior in the PAD process [40]. NVP/C powders were ball milled in cyclohexane to obtain suitable PSD. Figure 2c shows the unimodal PSD of NVP/C powder after the milling process at 300 rpm for 2 h, with a d_{50} value of 2 µm.

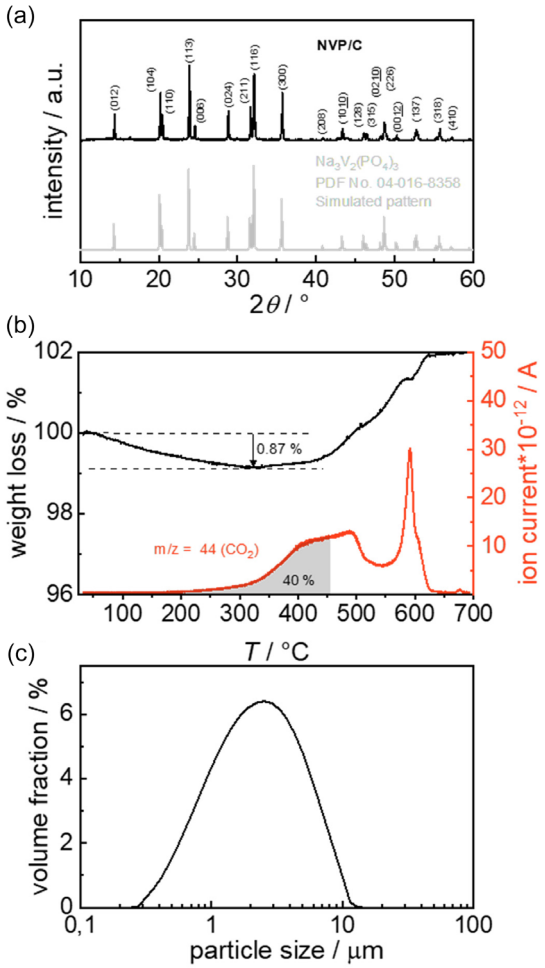

FIGURE 2 | (a) X-ray diffraction patterns, and (b) thermogravimetric analysis coupled with mass spectrometry of as produced NVP/C composite powders, (c) PSD of milled composite powders for PAD.

3.2 | Tape-Cast and Powder Aerosol Deposited NVP/C Electrodes

The dimensions of the aluminum CCs and the CAM loading on these CCs are shown in Table 2. The CAM loading of the PAD electrodes was determined by weighing the polished aluminum substrates before and after the deposition process using a balance (Sartorius La 110 S Master Pro). Additionally, to assess the CAM loading of tape-cast electrodes, three pieces (Ø13 mm) were punched from the uncoated part of the aluminum foil and weighed. The mean empty weight of the aluminum foil was subtracted from the weight of coated foils. As shown in Table 2, the CAM loading of tape-cast, 1st and 2nd set of PAD electrodes were 2.9 ± 0.2 mg cm^{-2}, 4.7 ± 0.7 mg cm^{-2}, and 9.2 ± 1 mg cm^{-2}, respectively.

The difference in CAM loading between the 1st and 2nd set of powder aerosol deposited electrodes can be explained by the particle-substrate interactions with respect to the velocity of the supplied gas [37]. The kinetic energy of particles directed toward the substrate is directly related to gas flow toward the aerosol chamber. Higher gas velocities can lead to agglomeration of the particles in the aerosol chamber, and when these agglomerates hit the substrate, a portion of the kinetic energy to break up the agglomerates is lost. In this case, the build-up of the anchor layer and subsequent layers at each pass may be hindered, resulting in a decreasing deposition rate. Therefore, the parameters, such as particle size and gas velocity must be carefully adjusted for successful deposition. The reduced gas flow for the 2nd set of powder aerosol deposited electrodes production might have led to a more stable aerosol. As a result of that, electrodes with higher CAM loadings were obtained, even with a fewer number of scans in the PAD process (Table 1).

Cross-section SEM images of the NVP/C electrodes are shown in Figure 3. The tape-cast NVP/C layer on 15 µm thick Al foil is also about 15 µm (Figure 3a). The tape-cast layer appears grainy and porous. The integrity of the layer is good with favorable contact to the Al foil. The powder aerosol deposited layer in the as-deposited state shows loose contact on 300 µm thick Al substrate, which we attribute to the grinding process for SEM preparation (Figure 3b). It is assumed that the microstrain in the as-deposited nano-structured layers causes cracks and contact loss during the preparation process. The annealed 1st set of PAD-NVP/C layer, on the contrary, shows excellent contact with the Al substrate without any cracks, and it appears to be a dense cathode layer (Figure 3c). The thickness of the 1st set of PAD-NVP/C cathode layers is about 20 µm. It can be seen from Figure 3d,e that the 2nd set of PAD-NVP/C electrodes are thicker compared to the 1st set, which are about 40 µm. Figure 3 supports the CAM loading results. Vertical and horizontal cracks are present, and we believe they are due to the preparation process.

The X-ray diffraction patterns of the powder aerosol deposited films on Al substrates are shown in Figure 4. The reflections with dashed lines and Miller indices belong to the Al substrate. The rest of the reflections agree with the reference pattern shown in the figure with the PDF number 04-016-8358. It can be concluded that the NVP structure was preserved in the deposition process. The main phase was also maintained after the posttreatment

TABLE 2 | Physical properties of tape-cast and powder aerosol deposited round shaped electrodes.

	Aluminum Substrate			CAM	
Type	**Thickness (µm)**	**Diameter (mm)**	**Area (cm^2)**	**CAM weight (mg)**	**CAM loading (cm^{-2})**
Tape-cast	15	13	1.33	4.5 ± 0.3	3.4 ± 0.2
PAD – 1st set	300	10	0.79	3.9 ± 0.6	4.7 ± 0.7
PAD – 2nd set	300	10	0.79	7.2 ± 0.8	9.2 ± 1

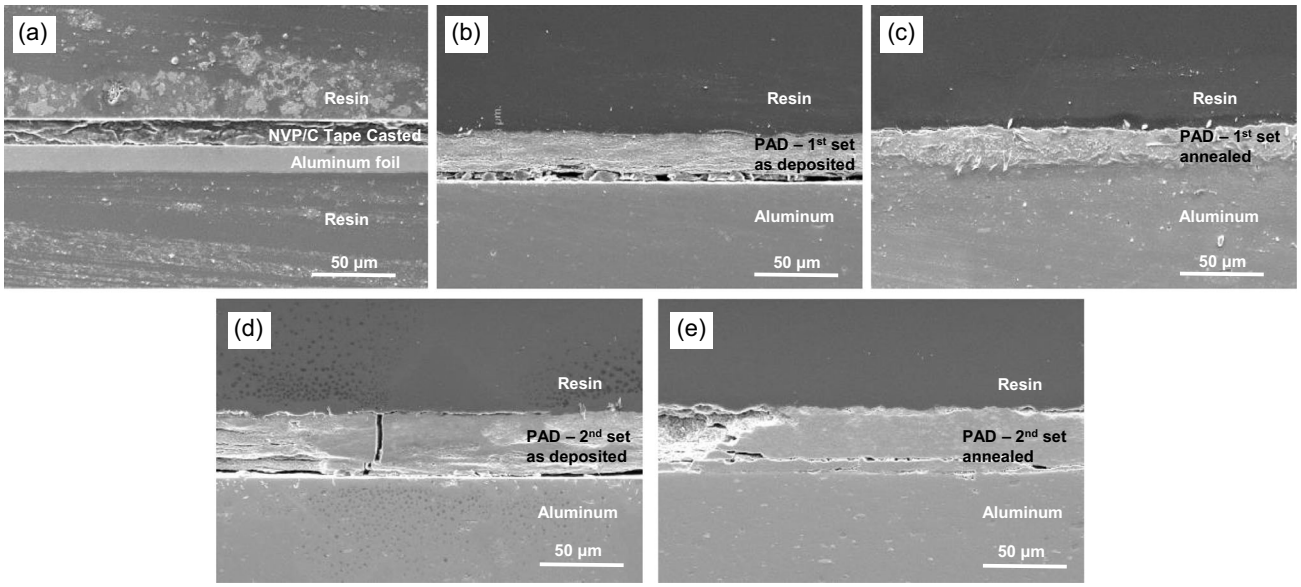

FIGURE 3 | Cross-sectional SEM images of NVP/C electrodes; (a) Tape-cast NVP/C on aluminum foil, 1st set of PAD-NVP/C cathodes in (b) as-deposited and (c) annealed (250°C) state, 2nd set of PAD-NVP/C cathodes in (d) as-deposited, and (e) annealed (250°C) state.

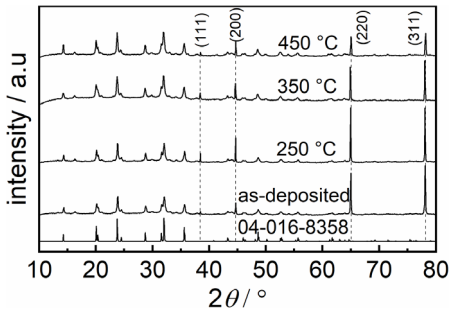

FIGURE 4 | X-ray diffraction diagram of NVP/C electrodes deposited on Al substrates without posttreatment (as-deposited) and after annealing (T_a = 250°C, 350°C, and 450°C). The pattern at the bottom belongs to reference simulated pattern from the PDF No. 04-016−8358.

between 250°C and 450°C of the powder aerosol deposited layers on the Al substrate.

Rietveld refinement plots of the synthesized powder and the as-deposited PAD-NVP/C cathode layer are displayed in Figure 5 as examples. Refinement plots of the other annealed PAD-NVP/C cathodes and structural information derived from the refinement can be found in the Supporting Information (Figure S2) and (Tables S1–S5), respectively. The sharp reflections in Figure 5b belong to the aluminum substrate. The reflections from substrate material were excluded in the refinement. As a consequence, sharp peaks appear in the blue difference line in Figure 5b. The substrate material reflections do not overlap with the main reflections of the CAM. Therefore, only the NVP reflections are targeted in order to maintain a stable refinement. The reflections of NVP in powder form appear as sharp peaks which indicates high crystallinity. In contrast, the powder aerosol deposited cathode material exhibits broadened reflections, indicating smaller crystallite size in the deposited cathode layer.

Crystallite size and microstrain of the annealed PAD cathode layers, as well as the powder, are summarized in Table 3. It is confirmed by Rietveld refinement that the large crystallites in powders are drastically decreased when they are powder aerosol deposited. This is an expected result due to the "Room Temperature Impact Consolidation" (RTIC) mechanism explained by Akedo et al. [20] during the PAD. An increasing crystallite size with increasing annealing temperature was not observed. This is mainly because even 450°C is insufficient to promote a crystallite growth. The maximum annealing temperature was opted as 450°C to prevent the aluminum substrate material, which has a melting temperature of 660°C, from melting or becoming excessively soft. Microstrain in the PAD-NVP films also remains more or less unchanged with the increasing annealing temperature.

3.3 | Electrochemical Properties of NVP/C Electrodes

The discharge capacities of the tape-cast and the 1st set of PAD-NVP/C electrodes in half cells versus Na metal are shown in

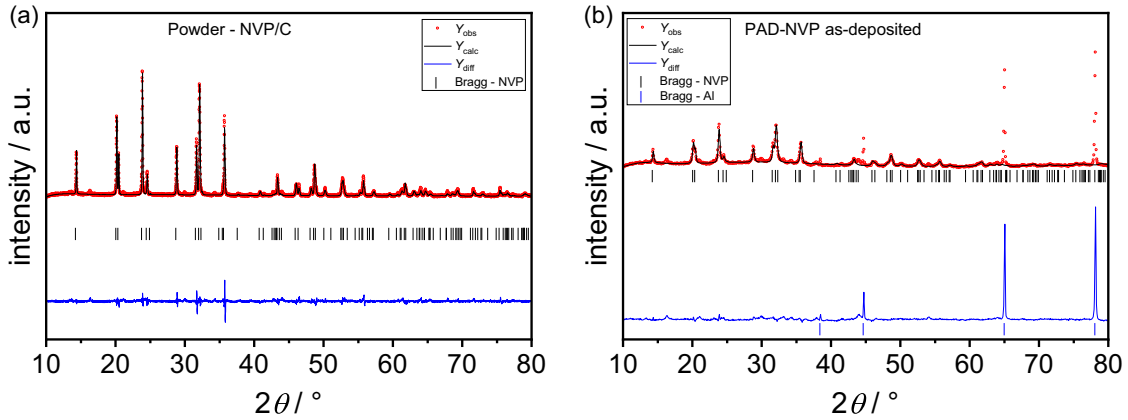

FIGURE 5 | Rietveld refinement of (a) as synthesized NVP/C powder and (b) powder aerosol deposited NVP/C cathode film on Al substrate (Bragg positions of aluminum were added beneath the blue difference line).

TABLE 3 | Rietveld analysis results of powder aerosol deposited NVP/C composite cathode materials on Al substrates.

Type	Sample	Crystallite size (nm)	Microstrain (%)
Powder	NVP/C	413 ± 31	0.13
PAD film	as deposited	49 ± 12	0.33
PAD film	annealed @250°C	56 ± 13	0.25
PAD film	annealed @350°C	45 ± 8	0.30
PAD film	annealed @450°C	65 ± 13	0.37

Figure 6. Cycling was performed between 1.5–4.5 V for 20 cycles at a C-rate of C/10. The tape-cast electrodes exhibit a discharge capacity of 90 mAh g^{-1}, with the shaded area indicating the standard deviation for each cycle in Figure 6a.

The as-deposited PAD-NVP/C electrode (filled triangle symbol) shows an initial discharge capacity of 40 mAh g^{-1}, which decreases to 24 mAh g^{-1} by the fifth cycle, after which the capacity remains stable. This reduced performance can be attributed to the nanocrystalline structure and high internal microstrain introduced during the PAD process [39]. The high-velocity particle impacts inherent to room-temperature impact consolidation cause plastic deformation of fractured particles and create residual stress within the deposited film [20]. These microstructural aspects impedes ion mobility due to increased grain boundary densities within the deposited cathode layer.

Thermal posttreatment is known to relieve microstrain and promote crystallite growth in PAD films [22], leading to improved ion transport. The annealed PAD-NVP/C electrode (unfilled triangle symbol) clearly reflects this effect and delivers a significantly higher initial specific discharge capacity of 76 mAh g^{-1}. The CAM loadings of the 1st set of as-deposited and annealed PAD electrodes are 5 and 4.7 mg cm^{-2}, respectively. Their corresponding discharge curves are shown in Figure 6b,c.

The coulombic efficiencies (CE) of the tape-cast and 1st set PAD-NVP/C electrodes in as-deposited and annealed states are shown in Figure 6a and are approximately 98%, 95% and 98%, respectively. The relatively low CE during the initial cycles are attributed to the solid electrolyte interphase (SEI) formation [41].

The cycling behavior of the PAD-NVP/C layers at increased current loads is shown in Figure 7. The C-rate was gradually increased from C/10 to 10C in steps of five cycles and then reduced back to C/10 for the final five cycles to evaluate capacity retention. As the C-rate increases, a capacity drop is observed, which can be attributed to increasing ohmic losses [42]. This effect becomes particularly pronounced at high current densities, where the delivered capacity approaches zero at 5C and 10C due to the high resistance and ionic transport limitations in the dense PAD cathode layers. The annealed PAD-NVP/C electrode shows slightly higher specific discharge capacities compared to the as-deposited electrode at low C-rates, consistent with reduced microstrain and improved transport after posttreatment. For both electrodes, the discharge capacity recovers when the C-rate is returned to C/10 during the final cycling sequence.

The second set of PAD-NVP/C electrodes was fabricated with a CAM loading of ~10 mg cm^{-2}, resulting in substantially thicker layers compared to the first set (~4.7 mg cm^{-2}). These electrodes were posttreated between 250°C to 450°C in 100°C increments for 20 min dwell time. Electrochemical testing was performed between 2–4 V at a C-rate of C/10 for 20 cycles.

Figure 8a shows that the thicker PAD electrodes deliver significantly lower specific discharge capacities than the thinner ones shown in Figure 6. In the as-deposited state, only ~1–1.5 mAh g^{-1} of specific discharge capacity can be delivered. Posttreatment leads to a slight improvement in specific discharge capacity as the annealing temperature increases from 250°C to 450°C, but the overall values remain low. Figure 8b highlights the effect of CAM loading in the as-deposited state: while a PAD electrode with 5 mg cm^{-2} delivers 27 mAh g^{-1}, the electrode with 11 mg cm^{-2} delivers almost no capacity. Even after annealing (Figure 8c), thicker PAD layers deliver less charge than thinner ones.

Although fabricating PAD electrodes with higher CAM loadings is possible, their transport properties deteriorate due to microstructural constraints. Because PAD produces dense films [37], increasing the layer thickness increases the diffusion path length and further restricts electrolyte access to the active material. As a result, cathode utilization decreases significantly as PAD layer thickness increases. The corresponding discharge curves of the

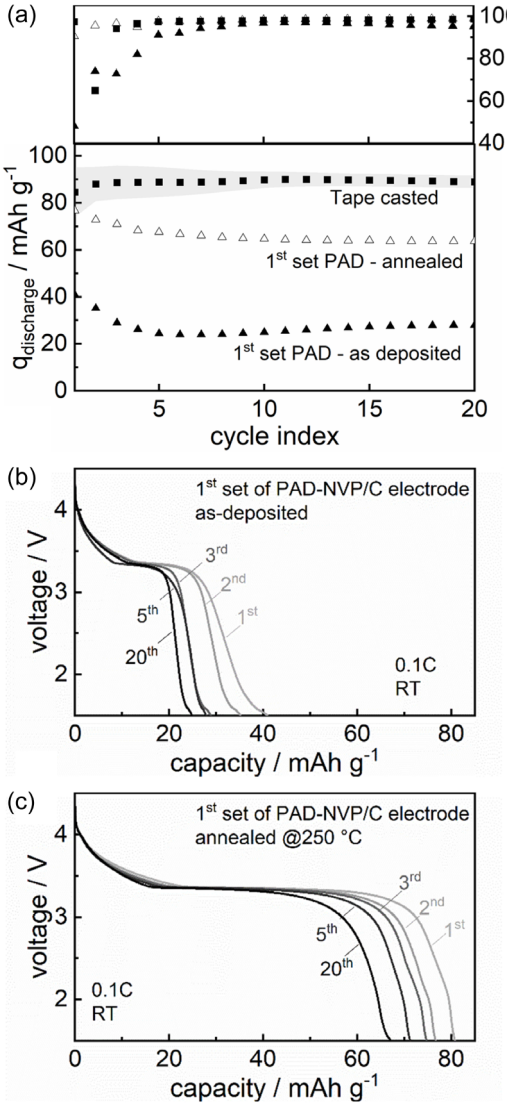

FIGURE 6 | (a) Specific discharge capacities of NVP/C electrodes at a C-rate of C/10 for 20 cycles between 1.5–4.5 V; tape-cast ('■') and 1st set of PAD-NVP/C electrodes in as deposited ('▲') and annealed ('Δ') states. Voltage vs. discharge capacity curves for (b) as-deposited and (c) annealed (T_a = 250°C) 1st set of PAD-NVP/C electrodes. The corresponding coulombic efficiencies (CE) of the respective electrodes are overlaid on the specific discharge capacity plot using the same symbols.

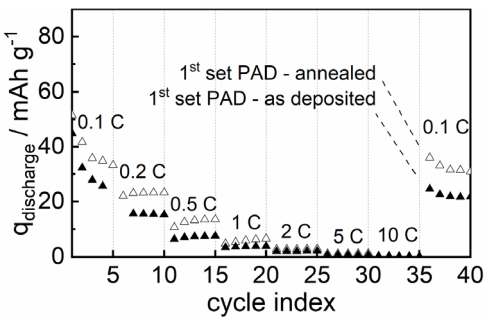

FIGURE 7 | Rate capability of as-deposited and annealed PAD NVP/C electrodes at different C-rates; C/10, C/5, C/2, 1C, 2C, 5C, and 10C for five cycles at each C-rate between 1.5 and 4.5 V.

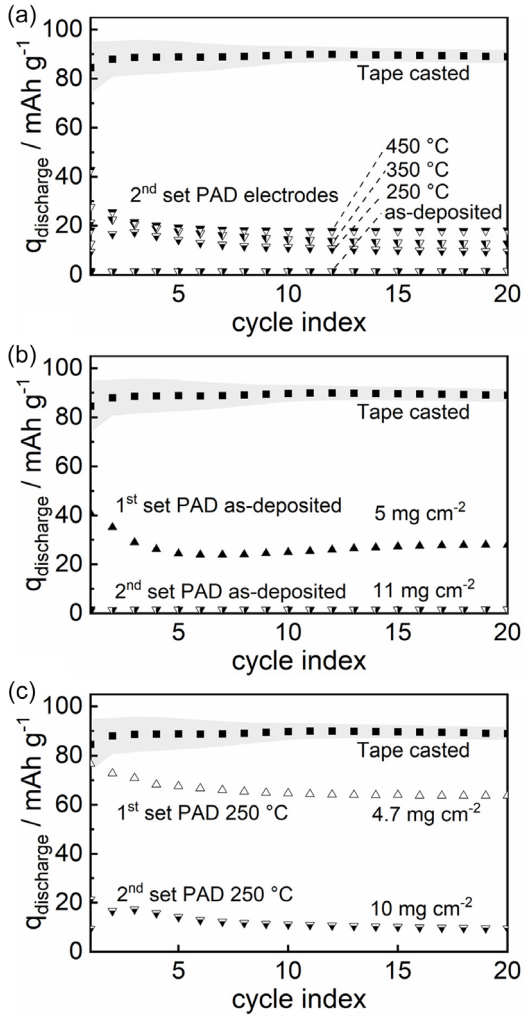

FIGURE 8 | Specific discharge capacities of (a) the 2nd set of powder aerosol deposited electrodes, (b) the 1st and 2nd set of PAD-NVP/C electrodes in as deposited state, (c) the 1st and 2nd set of PAD-NVP/C electrodes in annealed (250°C) state. The tape-cast electrodes are shown for comparison. CAM loading of the respective electrodes is given in the figures.

second set of PAD electrodes are provided in the Supporting Information (Figure S4).

A discrepancy in specific discharge capacities of the 1st set of PAD-NVP/C annealed cathodes is noticeable in Figures 6a and 7. Under standard cycling conditions (constant C-rate of C/10, Figure 6a), the specific discharge capacity initially reached 76 mAh g^{-1} and decreasing to 67 mAh g^{-1} by the fifth cycle. In contrast, the identical cathode type subjected to the rate capacity protocol (Figure 7) showed only 51 mAh g^{-1} at C/10, dropping rapidly to 33 mAh g^{-1} after five cycles. To elucidate this discrepancy, the charge extracted from PAD-NVP/C composite cathodes was evaluated as a function of the active material loading (Figure 9), rather than as a specific discharge capacity as shown in Figures 6a and 7.

Figure 9a shows the mean delivered charge during the first five discharge steps and their standard deviation as error bars. The delivered charge remains nearly constant (~0.15–0.18 mAh) across the range of investigated CAM loadings with no clear proportional increase with increasing mass or thickness (upper *x*-axis). Figure 9b

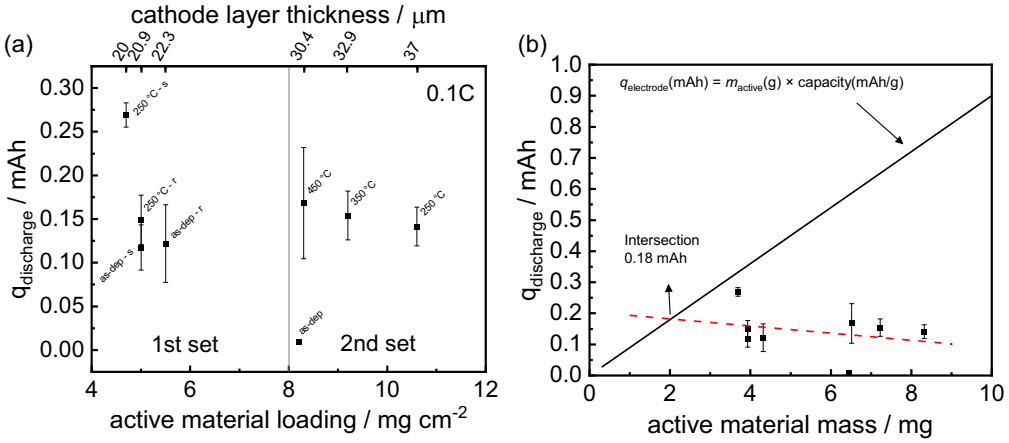

FIGURE 9 | (a) Charge extracted from PAD-NVP/C cathodes as a function of CAM loading on Al substrates. Corresponding layer thickness is shown on the upper *x*-axis. Data labeled 's' correspond to standard C/10 cycling protocol, while '*r*' represent the first five cycles at C/10 from the rate capability procedure. (b) Charge extracted from PAD-NVP/C cathodes vs. active material mass. The continuous black line indicates the ideal trend for a porous tape-cast cathode, while the dashed red line is a linear fit to the PAD data.

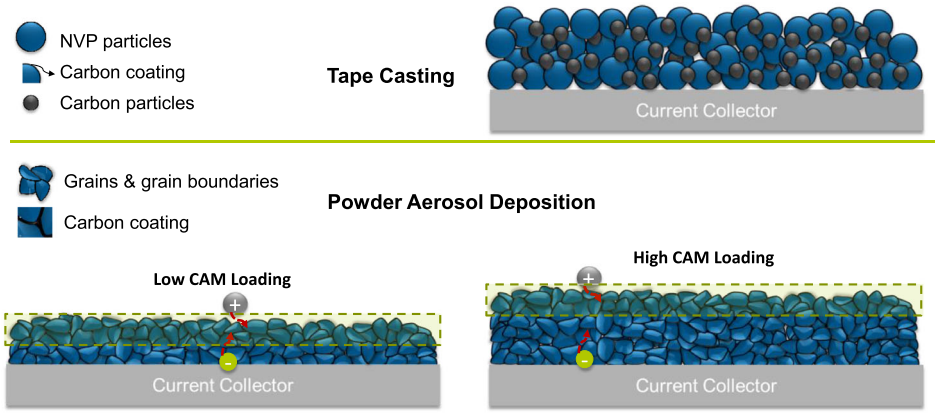

FIGURE 10 | Schematic depiction of cross-section of tape-cast and powder aerosol deposited electrodes with high and low CAM loading.

visualizes the same dataset plotted against the active material mass. A linear trend line (dashed red) was fitted to the charge extracted from all PAD composite cathodes. The continuous straight line represents the expected ideal trend for a porous tape-cast cathode, where the delivered charge is proportional to active material mass, assuming a practical NVP/C capacity of 90 mAh g^{-1} (based on tape-cast data in Figure 6a). In principle, the delivered charge should be proportional to the active mass in a fully accessible porous electrode. However, PAD cathodes exhibit much weaker dependence on active mass loading.

We emphasize that this apparent limitation of extractable charge is an electrochemical observation and does not directly correspond to a depth-resolved utilization profile. While the dense, pore-free microstructure of PAD films likely restricts electrolyte penetration, confirmation of the extent to which the active material participates at different depths would require compositional or chemically sensitive depth-profiling techniques such as glow discharge optical emission spectroscopy [43] or time-of-flight secondary ion mass spectrometry [44, 45]. Therefore, the hypothesis that only the near-surface region participates in de-/intercalation should be regarded as supported by the observed electrochemical trend, but not as a proven mechanistic conclusion.

4 | Discussion

In Figure 10, cross-sectionals of tape-cast and powder aerosol-deposited electrodes are schematically depicted. Conventional tape-cast electrodes exhibit a porous microstructure, where particle–particle contact is relatively poor and conductive additives are homogeneously dispersed throughout the layer. In contrast, PAD electrodes form dense pore-free layers composed of densely connected nanograins and grain boundaries after room temperature impact consolidation [46, 47]. This process fractures and refines the incoming particles, reducing grain size significantly. Although PAD films provide improved contact with the Al CC, their cathode utilization remains limited. The dashed regions in Figure 10 indicate the portion of the PAD cathode that is electrochemically accessible. For low CAM loading, this active region is closer to the CC, reducing electron transport distances. However, for high CAM loading, both electrons and ions must traverse significantly longer paths in a dense nanostructured environment, leading to reduced utilization.

Unlike tape-cast electrodes, which typically contain ~10 wt.% conductive additive, the PAD-NVP/C electrodes in this study were intentionally deposited without any additional carbon additives. This deliberate choice reflects an advantage of the PAD

method, namely, the ability to fabricate functional cathode layers without binder or conductive additives. The NVP/C powder used in this study contains ~2.2 wt.% carbon. This is much lower than typical tape-cast cathodes where additional carbon is physically added. The final carbon distribution after PAD is not precisely known. Linz et al. [48] investigated the deposition behavior of core–shell ceramic particles (Al_2O_3-core, SiO_2-shell, and NMC-core, $LiNbO_3$-shell) to reveal the underlying PAD-mechanism. As a result of the analyses, energy-dispersive X-ray spectroscopy, and scanning transmission electron microscopy, it was observed that shell materials significantly get enriched in the resulting layers. This implies that particles undergo fragmentation upon impact and predominantly shell-derived fragments contributing to film formation. Therefore, adapting this finding to deposition of the core-shell carbon coated NVP powders, it can be assumed that resulting carbon content in PAD-NVP films might be slightly higher than actual carbon content of NVP/C powders.

Soundaraj et al. [49] reported the effect of carbon content on the transport properties of NVP/C composites and showed the importance of carbon, which determines whether the limiting factor is the ionic or electronic conductivity. They found that NVP/C with <0.1 wt.% carbon exhibits predominantly ionic conductivity ($\sim 2 \times 10^{-6}$ S cm^{-1}), on the contrary, carbon content >1 wt.% produce a percolated amorphous carbon network that increases electronic conductivity up to 0.2 mS cm^{-1} without affecting ionic conductivity.

In the light of the above facts, our results suggest that the PAD films contain a sufficiently interconnected carbon network to support electronic conduction when we consider the carbon content exceeds 2 wt.% in our PAD-NVP/C layers. Nevertheless, the present study does not provide direct electronic conductivity measurements to separate ionic and electronic contributions. Therefore, also based on the microstructural features observed by SEM and on the electrochemical results, we believe ionic transport limitations are the dominant factor in limiting the capacity utilization of PAD-NVP/C electrodes. Further electrochemical impedance analyses are required to definitively confirm this hypothesis. Rietveld refinement results also confirm that crystallite size was reduced in PAD cathodes, which leads to an increased number of grain boundaries in the PAD-NVP cathode layers. Consequently, the increased number of grain boundaries may hinder ion transportation in the PAD cathodes.

Recent studies showed that the origin of grain boundary ionic resistance in oxide SEs is strongly material dependent [50–54]. For NaSICON systems where the ionic conduction occurs in an open 3D framework, Liu et al. [55] showed that the grain boundaries are highly resistive due to thermal expansion anisotropy between the a- and c- axes which causes microcracks and insufficient grain-grain contact at the grain boundaries during cooling. Therefore, the grain boundaries become rate-limiting conduction factor. In contrast, Kawahara et al. [56] reported that in the double perovskite (La, Li)NbO_3, the grain boundary ionic conductivity is three times higher than the bulk, and this unusual behavior originates from the absence of La enrichment at the boundary which is typically observed in LLTO; thereby producing boundaries that act as fast conduction pathways rather than blocking regions.

Wu and Guo [57] explained the grain-boundary blocking effect mechanism in the perovskite superionic conductor where ionic conduction is mostly 2D by vacancy hopping through bottlenecks. They attribute the effect primarily to a space-charge/depletion layer mechanism at the grain boundaries, which leads to dramatically reduced ion concentration and mobility in the boundary region compared to the bulk. These depleted regions act as high resistance barriers to ion transport, and resulting in grain boundary conductivities several orders of magnitude lower than the bulk.

Although there is ongoing debate regarding the contribution of grain boundaries versus pathways in the bulk to fast ion transport in bulk ceramic ion conductors, when it comes to the functional properties of PAD ceramic films, Exner et al. [58] showed that the functional properties of PAD ceramic films such as ionic/electronic conductivity, permittivity, polarization, and magnetization are substantially reduced in the as-deposited state. The room-temperature impact consolidation inherent to PAD produces a highly nanocrystalline microstructure characterized by severe lattice distortion, high internal strain, and partially amorphous or damaged regions, which collectively suppress intrinsic bulk functional behavior. Thermal posttreatment is therefore required to relax strain, heal damaged domains, restore crystallinity, and promote grain growth, thereby mitigating grain boundary blocking and enabling PAD layers to recover toward bulk-like performance.

In the present PAD-deposited NVP/C films, the nanocrystalline microstructure and reduced crystallite size revealed by Rietveld refinement suggest a high density of grain boundaries. While such features may plausibly contribute to the increased internal resistance, our study does not provide direct electrochemical separation of bulk and grain-boundary contributions. Therefore, we present the influence of grain-boundaries as a hypothesis consistent with the observed microstructure and crystallite size and microstrain calculated from Rietveld analyses.

Recent work on NVP-based polyanionic cathodes has shown that Na^+ transport and multielectron redox behavior are governed not only by macroscopic factors such as cathode thickness and porosity but also by local structural and chemical complexity. High-entropy substituted NVP phases, for example, exhibit enhanced kinetics and stabilized V^{2+}/V^{5+} multielectron reaction by tuning the local coordination environment and defect landscape, as revealed by in situ XRD and (XANES)_X-ray absorption near edge structure studies [4]. Likewise, a recent review on high-voltage V^{4+}/V^{5+} redox in NVP-based cathodes emphasizes that Na^+ migration pathways, redox activity, and structural stability are strongly coupled within the NaSICON framework [6]. Yilin et al. [59, 60] demonstrated that in polyanion-type electrode structures, the migration of Na^+ ions occurs via multistep hopping processes involving transient coordination changes and local lattice rearrangements, rather than simple bulk diffusion along rigid pathways. The incorporation of conductive MXene nanosheets introduces adaptive interfaces, both structurally and electronically, that regulate Na^+ transport by providing low-energy adsorption sites that facilitate rapid Na^+ exchange. These insights suggest that, in dense PAD-processed NVP/C cathodes, the nanocrystalline, strained microstructure and PAD-induced local disorder may further hinder the Na^+ migration beyond the simple concept of transport occurring either in the bulk or at the grain boundaries. While our current study does not directly investigate such local coordination changes, the significant dependence of thickness and the apparent limit of extracted charge are consistent with a hypothesis in which

macroscopic factors (such as electrolyte access and diffusion length) and microscopic factors (such as local structure and defect configuration) collectively restrict Na^+ transport in thick PAD films.

In contrast, the dense microstructure of PAD cathodes prevents the liquid electrolyte from penetrating deeply into the layer, which further increases cell resistance and deteriorates ion transport. This has a detrimental effect on the transport properties. As a result, only the upper surface region of the PAD layer is in effective contact with the electrolyte. The absence of open porosity hinders the wetting of the powder aerosol deposited electrode, which severely limits the electrochemically active area. Figure 9 supports the hypothesis that only a limited fraction of the PAD cathode layer near the surface is electrochemically accessible. Beyond a certain thickness, the utilization of PAD cathodes becomes constrained due to ion-transport and diffusion limitations in the dense, low-porosity layer, which restricts liquid electrolyte penetration. To estimate this limiting thickness, we intersect the fitted linear line (dashed red, Figure 9b) of the charge extracted from PAD cathodes with the idealized linear trend (continuous black, Figure 9b) expected from a porous tape-cast cathode. The intersection point ($\sim$2 mg, $\sim$0.18 mAh) provides an estimate of the maximum active material mass that can be effectively utilized within the PAD layer. This implies that below $\sim$2 mg of active material mass (which corresponds to a CAM loading of 2.5 mg cm^{-2} on Al substrates with Ø10 mm), the calculated specific discharge capacities represent reliable utilization. In contrast, above this threshold, the term "specific discharge capacity" becomes misleading, as a significant fraction of the active mass cannot participate in de/-intercalation. In other words, we hypothesize that only a thin PAD deposited layer from top contributes to the reversible capacity of the PAD-NVP composite cathodes that are investigated here.

Among other uncontrolled factors, mechanical contact issues and wetting heterogeneity may influence the accessible electrochemical area, particularly if microcracks form within the dense PAD cathode layers during the cell assembly or de-/intercalation reactions. Thus, the forementioned discrepancy reflects the combined effect of the intrinsic charge utilization limit of PAD films and possible assembly-related factors.

5 | Conclusions

High active material loading powder aerosol deposited NVP/C cathodes were successfully fabricated directly on Al substrates without the use of binder or solvent, and their electrochemical behavior was benchmarked against tape-cast electrodes. Posttreatment significantly improves their performance: initial specific discharge capacity increases from $\sim$40 mAh g^{-1} in the as-deposited state to $\sim$76 mAh g^{-1} after annealing, approaching the $\sim$90 mAh g^{-1} obtained from tape-cast cathodes.

The results indicate that the dense, nanostructured PAD microstructure restricts liquid electrolyte penetration and ionic transport, leading to incomplete utilization of the active material, particularly at higher cathode loadings. The extractable charge from the PAD electrodes remains nearly independent of CAM mass, demonstrating that only a limited fraction participates in reversible de/-intercalation, which we suggest may be the near-surface region in direct contact with the electrolyte. As a result, specific capacity fails to reflect the true utilization once the CAM loading exceeds $\sim$2 mg in PAD electrodes.

These observations point to transport-related constraints as the dominating limitations in thick PAD cathode layers. Future improvements to PAD-based cathodes will require strategies that more directly address the transport limitations identified in this work. Potential approaches include increasing the carbon content of the starting powder to strengthen the electronic percolation network, as well as introducing controlled porosity (e.g., polymer sacrificial templating) to promote electrolyte infiltration, or incorporating solid electrolyte phases by PAD co-deposition to support ion transport within the dense layer. Resolving ionic and electronic contributions separately and understanding diffusion-based properties is also essential for future work to enable effective utilization of active material in thick PAD films.

Nanometer-thick PAD cathodes reported to date remain far from the actual industry applications. However, we demonstrated that powder aerosol deposited cathode layers with high CAM loading may bridge the gap toward practical applications. The ensuing challenges with this approach are identified. The major obstacles to the industrial implementation of PAD cathodes are revealed. This study identifies the key challenges for PAD of electrode materials to become a viable future route.

Author Contributions

Mutlucan Sozak, **Sofie Knies**, **Matteo Bianchini**, and **Ralf Moos:** conceptualization and methodology. **Mutlucan Sozak** and **Sofie Knies:** investigation. **Matteo Bianchini** and **Ralf Moos:** validation. **Matteo Bianchini** and **Ralf Moos:** supervision and funding acquisition. **Mutlucan Sozak:** writing – original draft. **Matteo Bianchini** and **Ralf Moos:** writing – review and editing.

Acknowledgments

The authors are grateful to the KeyLab Electron and Optical Microscopy of the Bavarian Polymer Institute (BPI) for the SEM images, to G. Jena of the Chair of Applied Mechanics and Fluid Mechanics (J. Sesterhenn) for the particle size distribution measurements, to G. Zheleznov of the Chair of Inorganic Active Materials for Electrochemical Energy Storage (M. Bianchini), and to L. Geiling of the Chair of Electrochemical Process Engineering (C. Roth for the TG-MS measurements, to the Chair of Metals and Alloys (U. Glatzel) for enabling the XRD measurements, to Dr. Mainul Akhtar for initial discussions on cathode active material synthesis and providing powder for preliminary studies.

Open Access funding enabled and organized by Projekt DEAL.

Funding

This study was funded by the Deutsche Forschungsgemeinschaft (DFG, German Research Foundation) - 508497297. Support by the BayBatt Cell Technology Center is gratefully acknowledged, funded by the Deutsche Forschungsgemeinschaft (DFG, German Research Foundation) - INST 91/452-1 LAGG.

Conflicts of Interest

The authors declare no conflicts of interest.

Data Availability Statement

The data presented in this study are available on request.

References

1. P. K. Nayak, L. Yang, W. Brehm, and P. Adelhelm, "From Lithium-Ion to Sodium-Ion Batteries: Advantages, Challenges, and Surprises," *Angewandte Chemie International Edition* 57, no. 1 (2018): 102–120, https://doi.org/10.1002/anie.201703772.

2. J. L. Murray, "The Al–Na (Aluminum-Sodium) System," *Bulletin of Alloy Phase Diagrams* 4, no. 4 (1983): 407–410, https://doi.org/10.1007/BF02868094.

3. Y. Uebou, T. Kiyabu, S. Okada, and J. I. Yamaki, *Electlochemical Sodium Insertion Into the 3D-Framework of $Na_3M_2(PO_4)_3$ (M = Fe, V)*, Vol. 16 (The Reports of Institute of Advanced Material Study, Kyushu University, 2002), 1–5, https://doi.org/10.15017/7951.

4. Z. Hao, X. Shi, W. Zhu, et al., "Boosting Multielectron Reaction Stability of Sodium Vanadium Phosphate by High-Entropy Substitution," *ACS Nano* 18, no. 13 (2024): 9354–9364, https://doi.org/10.1021/acsnano.3c09519.

5. X. Liao, Y. Li, B. Xie, et al., "Unlocking Advanced Sodium Storage Performance: High-Entropy Modulates Crystallographic Sites With Reversible Multi-Electron Reaction," *Energy Storage Materials* 74 (2025): 103920, https://doi.org/10.1016/j.ensm.2024.103920.

6. M. Zhou, X. Zhou, L. Li, X. Chen, Z. Qiao, and S. Chou, "Emerging High Voltage V^{4+}/V^{5+} Redox Reactions in $Na_3V_2(PO_4)_3$-Based Cathodes for Sodium-Ion Batteries," *Chemical Science* 15, no. 23 (2024): 8651–8663, https://doi.org/10.1039/D4SC01226G.

7. T. Or, S. W. D. Gourley, K. Kaliyappan, Y. Zheng, M. Li, and Z. Chen, "*Recent Progress in Surface Coatings for Sodium-Ion Battery Electrode Materials*," *Electrochemical Energy Reviews* 5(Suppl1), no. 20 (2022), https://link.springer.com/article/10.1007/s41918-022-00137-7.

8. R. S. Kate, S. V. Kadam, M. V. Kulkarni, R. J. Deokate, B. B. Kale, and R. S. Kalubarme, "Highly Stable and Nanoporous $Na_3V_2(PO_4)_3$@C Cathode Material for Sodium-Ion Batteries Using Thermal Management," *Journal of Energy Storage* 74 (2023): 109245, https://doi.org/10.1016/j.est.2023.109245.

9. Z. Jian, L. Zhao, H. Pan, et al., "Carbon Coated $Na_3V_2(PO_4)_3$ as Novel Electrode Material for Sodium Ion Batteries," *Electrochemistry Communications* 14, no. 1 (2012): 86–89, https://doi.org/10.1016/j.elecom.2011.11.009.

10. S. Y. Gültekin, A. Güler, D. Kuruahmet, et al., "Graphene Aerogel-Supported $Na_3V_2(PO_4)_3$/C Cathodes for Sodium-Ion Batteries," *Diamond and Related Materials* 139 (2023): 110399, https://doi.org/10.1016/j.diamond.2023.110399.

11. R. S. Kate, K. Bhattacharjee, M. V. Kulkarni, B. B. Kale, R. J. Deokate, and R. S. Kalubarme, "Microstructure Tuned $Na_3V_2(PO_4)_3$@C Electrodes Toward Ultra-Long-Life Sodium-Ion Batteries," *RSC Advances* 14 (2024): 25062–25070, https://doi.org/10.1039/D4RA04221B.

12. S. Liu, Z. Xu, L. Ren, et al., "Fe-Modified NASICON-Type $Na_3V_2(PO_4)_3$ as a Cathode Material for Sodium Ion Batteries," *RSC Advances* 14, no. 7 (2024): 4835–4843, https://doi.org/10.1039/D3RA08714J.

13. P. Hu, T. Zhu, C. Cai, et al., "A High-Energy NASICON-Type $Na_{3.2}MnTi_{0.8}V_{0.2}(PO_4)_3$ Cathode Material With Reversible 3.2-Electron Redox Reaction for Sodium-Ion Batteries," *Angewandte Chemie* 135, no. 14 (2023): e202219304, https://doi.org/10.1002/ange.202219304.

14. D. Wang, X. Bie, Q. Fu, et al., "Symmetric Sodium-Ion Batteries With High Power and Long Lifespan," *Nature Communications* 8, no. 1 (2017): 15888, https://doi.org/10.1038/ncomms15888.

15. J. Cong, S. Luo, P. Li, K. Li, P. Li, and S. Yan, "Towards Enhanced Structural Stability by Investigation of the Mechanism of K Ion Doping in $Na_3V_2(PO_4)_3$/C for Sodium Ion Batteries," *Journal of Energy Storage* 72 (2023): 108808, https://doi.org/10.1016/j.est.2023.108808.

16. M. Akhtar, H. Arraghraghi, S. Kunz, Q. Wang, and M. Bianchini, "A Novel Solid-State Synthesis Route for High Voltage $Na_3V_2(PO_4)_2F_{3-2y}O_{2y}$ Cathode Materials for Na-Ion Batteries," *Journal of Materials Chemistry A* 11, no. 46 (2023): 25650–25661, https://doi.org/10.1039/D3TA04239A.

17. T. Akçay, M. Häringer, K. Pfeifer, et al., "$Na_3V_2(PO_4)_3$ —A Highly Promising Anode and Cathode Material for Sodium-Ion Batteries," *ACS Applied Energy Materials* 4, no. 11 (2021): 12688–12695, https://doi.org/10.1021/acsaem.1c02413.

18. F. Lalère, J. B. Leriche, M. Courty, et al., "An All-Solid State NASICON Sodium Battery Operating at 200°C," *Journal of Power Sources* 247 (2014): 975–980, https://doi.org/10.1016/j.jpowsour.2013.09.051.

19. J. Akedo, "Aerosol Deposition Method for Fabrication of Nano Crystal Ceramic Layer," *Materials Science Forum* 449–452 (2004): 43–48, https://doi.org/10.4028/www.scientific.net/MSF.449-452.43.

20. J. Akedo, "Room Temperature Impact Consolidation (RTIC) of Fine Ceramic Powder by Aerosol Deposition Method and Applications to Microdevices," *Journal of Thermal Spray Technology* 17, no. 2 (2008): 181–198, https://doi.org/10.1007/s11666-008-9163-7.

21. C.-W. Ahn, J.-J. Choi, J. Ryu, et al., "Microstructure and Ionic Conductivity in $Li_7La_3Zr_2O_{12}$ Film Prepared by Aerosol Deposition Method," *Journal of the Electrochemical Society* 162 (2014): A60–A63, https://doi.org/10.1149/2.0411501jes.

22. D. Hanft, J. Exner, and R. Moos, "Thick-Films of Garnet-Type Lithium Ion Conductor Prepared by the Aerosol Deposition Method: The Role of Morphology and Annealing Treatment on the Ionic Conductivity," *Journal of Power Sources* 361 (2017): 61–69, https://doi.org/10.1016/j.jpowsour.2017.06.061.

23. D. Popovici, H. Nagai, S. Fujishima, and J. Akedo, "Preparation of Lithium Aluminum Titanium Phosphate Electrolytes Thick Films by Aerosol Deposition Method," *Journal of the American Ceramic Society* 94 (2011): 3847–3850, https://doi.org/10.1111/j.1551-2916.2011.04551.x.

24. R. Inada, K. Ishida, M. Tojo, T. Okada, T. Tojo, and Y. Sakurai, "Properties of Aerosol Deposited NASICON-Type $Li_{1.5}Al_{0.5}Ge_{1.5}(PO_4)_3$ Solid Electrolyte Thin Films," *Ceramics International* 41, no. 9 (2015): 11136–11142, https://doi.org/10.1016/j.ceramint.2015.05.062.

25. A. Khan, C.-W. Ahn, J. Ryu, et al., "Effect of Annealing on Properties of Lithium Aluminum Germanium Phosphate Electrolyte Thick Films Prepared by Aerosol Deposition," *Metals and Materials International* 20, no. 2 (2014): 399–404, https://doi.org/10.1007/s12540-014-1018-9.

26. I. Kim, J. Park, T.-H. Nam, et al., "Electrochemical Properties of An As-Deposited $LiFePO_4$ Thin Film Electrode Prepared by Aerosol Deposition," *Journal of Power Sources* 244 (2013): 646–651, https://doi.org/10.1016/j.jpowsour.2012.12.108.

27. R. Inada, K. Shibukawa, C. Masada, Y. Nakanishi, and Y. Sakurai, "Characterization of as-Deposited $Li_4Ti_5O_{12}$ Thin Film Electrode Prepared by Aerosol Deposition Method," *Journal of Power Sources* 253 (2014): 181–186, https://doi.org/10.1016/j.jpowsour.2013.12.084.

28. T. Yamamoto, H. Iwasaki, Y. Suzuki, et al., "A Li-Free Inverted-Stack All-Solid-State Thin Film Battery Using Crystalline Cathode Material," *Electrochemistry Communications* 105 (2019): 106494, https://doi.org/10.1016/j.elecom.2019.106494.

29. L. Hennerici, P. Ficht, M. Schamel, et al., "Lithium All-Solid-State Batteries Fabricated at Room Temperature by the Powder Aerosol Deposition Method with Garnet-Type Electrolyte and Graded Composite Cathode," *Advanced Materials Technologies* 10 (2025): 2400745, https://doi.org/10.1002/admt.202400745.

30. I. Kim, T. -H. Nam, K. -W. Kim, H .J. Ahn, et al., "$LiNi_{0.4}Co_{0.3}Mn_{0.3}O_2$ Thin Film Electrode by Aerosol Deposition," *Nanoscale Research Letters* 7 (2012): 64, https://doi.org/10.1186/1556-276X-7-64.

31. S. Iwasaki, T. Hamanaka, T. Yamakawa, et al., "Preparation of Thick-Film $LiNi_{1/3}Co_{1/3}Mn_{1/3}O_2$ Electrodes by Aerosol Deposition and Its Application to All-Solid-State Batteries," *Journal of Power Sources* 272 (2014): 1086–1090, https://doi.org/10.1016/j.jpowsour.2014.09.038.

32. E. J. Cheng, R. Oyama, T. Abe, and K. Kanamura, "High-Voltage All-Solid-State Lithium Metal Batteries Prepared by Aerosol Deposition," *Journal of the European Ceramic Society* 43 (2023): 2033–2038, https://doi.org/10.1016/j.jeurceramsoc.2022.12.023.

33. M. Sozak, T. Nazarenus, J. Exner, J. Kita, and R. Moos, "Room Temperature Manufacture of Dense NaSICON Solid Electrolyte Films for All-Solid-State-Sodium Batteries," *Journal of Materials Science* 58 (2023): 10108–10119, https://doi.org/10.1007/s10853-023-08642-w.

34. S. Teshima, Y. Ono, N. Goto, and R. Inada, "Electrical Conducting Properties of $Na_2Zn_2TeO_6$ Thick Films Fabricated by Aerosol Deposition," *Materials Letters* 324 (2022): 132640, https://doi.org/10.1016/j.matlet.2022.132640.

35. J. an Sam Oh, Q. Sun, C. Tian, et al., "Aerosol Deposited Freestanding $Na_3V_2(PO_4)_3$ Thin Film Micro Battery," *Materials Today Energy* 27 (2022): 101006, https://doi.org/10.1016/j.mtener.2022.101006.

36. X. Wang, R. A. P. Camacho, J. A. S. Oh, Y. F. Zhang, and L. Lu, "Improvement in the Electrode–electrolyte Interface of All-Solid-State Battery Using Aerosol Deposition Technology," *Functional Materials Letters* 16, no. 03n04 (2023): 2340003, https://doi.org/10.1142/S1793604723400039.

37. D. Hanft, J. Exner, M. Schubert, T. Stöcker, P. Fuierer, and R. Moos, "An Overview of the Aerosol Deposition Method: Process Fundamentals and New Trends in Materials Applications," *Journal of Ceramic Science and Technology* 6 (2015): 147–182, https://doi.org/10.4416/JCST2015-00018.

38. N. Doebelin and R. Kleeberg, "Profex: A Graphical User Interface for the Rietveld Refinement Program BGMN," *Journal of Applied Crystallography* 48 (2015): 1573–1580, https://doi.org/10.1107/S1600576715014685.

39. N. Van Nghia, S. Jafian, and I.-M. Hung, "Synthesis and Electrochemical Performance of the $Na_3V_2(PO_4)_3$ Cathode for Sodium-Ion Batteries," *Journal of Electronic Materials* 45 (2016): 2582–2590, https://doi.org/10.1007/s11664-016-4425-5.

40. J. Akedo and M. Lebedev, "Powder Preparation in Aerosol Deposition Method for Lead Zirconate Titanate Thick Films," *Japanese Journal of Applied Physics* 41, no. 1 (2002): 6980–6984, https://doi.org/10.1143/JJAP.41.6980.

41. M. Á. Muñoz-Márquez, D. Saurel, J. L. Gómez-Cámer, M. Casas-Cabanas, E. Castillo-Martínez, and T. Rojo, "Na-Ion Batteries for Large Scale Applications: A Review on Anode Materials and Solid Electrolyte Interphase Formation," *Advanced Energy Materials* 7, no. 20 (2017): 1700463, https://doi.org/10.1002/aenm.201700463.

42. G. Klinser, R. Zettl, M. Wilkening, H. Krenn, I. Hanzu, and R. Würschum, "Redox Processes in Sodium Vanadium Phosphate Cathodes - Insights From Operando Magnetometry," *Physical Chemistry Chemical Physics* 21, no. 36 (2019): 20151–20155, https://doi.org/10.1039/C9CP04045E.

43. M. Flügel, T. Waldmann, M. Kasper, and M. Wohlfahrt-Mehrens, "Detection of Copper Deposition on Anodes of Over-Discharged Lithium Ion Cells by GD-OES Depth Profiling," *ChemPhysChem* 21, no. 18 (2020): 2047–2050, https://doi.org/10.1002/cphc.202000333.

44. Y. You, A. Dolocan, W. Li, and A. Manthiram, "Understanding the Air-Exposure Degradation Chemistry at a Nanoscale of Layered Oxide Cathodes for Sodium-Ion Batteries," *Nano Letters* 19, no. 1 (2019): 182–188, https://doi.org/10.1021/acs.nanolett.8b03637.

45. J. R. Fitzpatrick, B. E. Murdock, P. K. Thakur, et al., "An in-Depth Study of the Solid Electrolyte Interphase Compositional Evolution in Sodium-Ion Batteries: Unravelling the Effects of a Na Metal Counter Electrode on the SEI," *Advanced Science* 12, no. 32 (2025): e04717, https://doi.org/10.1002/advs.202504717.

46. J. Exner, M. Schubert, D. Hanft, J. Kita, and R. Moos, "How to Treat Powders for the Room Temperature Aerosol Deposition Method to Avoid Porous, Low Strength Ceramic Films," *Journal of the European Ceramic Society* 39 (2019): 592–600, https://doi.org/10.1016/j.jeurceramsoc.2018.08.008.

47. J. Akedo, "Aerosol Deposition of Ceramic Thick Films at Room Temperature: Densification Mechanism of Ceramic Layers," *Journal of the American Ceramic Society* 89, no. 6 (2006): 1834–1839, https://doi.org/10.1111/j.1551-2916.2006.01030.x47.

48. M. Linz, F. Bühner, D. Paulus, et al., "Revealing the Deposition Mechanism of the Powder Aerosol Deposition Method Using Ceramic Oxide Core-Shell Particles," *Advanced Materials* 36, no. 7 (2024): e2308294, https://doi.org/10.1002/adma.202308294.

49. P. V. Soundaraj, E. Dashjav, D. Grüner, S. Prünte, C. Dellen, and F. Tietz, "Influence of Carbon Content on the Ionic and Electronic Conductivities of Dense $Na_3V_2(PO_4)_3$/C Composites," *Journal of Power Sources Advances* 26 (2024): 100144, https://doi.org/10.1016/j.powera.2024.100144.

50. Y. Inaguma, C. Liquan, M. Itoh, et al., "High Ionic Conductivity in Lithium Lanthanum Titanate," *Solid State Communications* 86, no. 10 (1993): 689–693, https://doi.org/10.1016/0038-1098(93)90841-A.

51. Y. Inaguma, L. Chen, M. Itoh, and T. Nakamura, "Candidate Compounds With Perovskite Structure for High Lithium Ionic Conductivity," *Solid State Ionics* 70-71 (1994): 196–202, https://doi.org/10.1016/0167-2738(94)90309-3.

52. R. Murugan, V. Thangadurai, and W. Weppner, "Fast Lithium Ion Conduction in Garnet-Type $Li_7La_3Zr_2O_{12}$," *Angewandte Chemie* 46 (2007): 7778–7781, https://doi.org/10.1002/anie.200701144.

53. C. R. Mariappan, M. Gellert, C. Yada, F. Rosciano, and B. Roling, "Grain Boundary Resistance of Fast Lithium Ion Conductors: Comparison Between a Lithium-Ion Conductive Li–Al–Ti–P–O-Type Glass Ceramic and a $Li_{1.5}Al_{0.5}Ge_{1.5}P_3O_{12}$ Ceramic," *Electrochemistry Communications* 14 (2012): 25–28, https://doi.org/10.1016/j.elecom.2011.10.022.

54. E. Lilley and J. E. Strutt, "Strutt: Bulk and Grain Boundary Ionic Conductivity in Polycrystalline β''- Alumina," *Physica Status Solidi A* 54, no. 2 (1979): 639–650, https://doi.org/10.1002/pssa.2210540227.

55. L. Liu, Q. Ma, X. Zhou, et al., "Simultaneously Improving Sodium Ionic Conductivity and Dendrite Behavior of NaSICON Ceramics by Grain-Boundary Modification," *Journal of Power Sources* 626 (2025): 235773, https://doi.org/10.1016/j.jpowsour.2024.235773.

56. K. Kawahara, R. Ishikawa, K. Nakayama, et al., "Fast Li-Ion Conduction at Grain Boundaries in (La, Li)NbO_3 polycrystals," *Journal of Power Sources* 441 (2019): 227187, https://doi.org/10.1016/j.jpowsour.2019.227187.

57. J.-F. Wu and X. Guo, "Origin of the Low Grain Boundary Conductivity in Lithium Ion Conducting Perovskites: $Li_{3x}La_{0.67-x}TiO_3$," *Physical Chemistry Chemical Physics* 19 (2017): 5880–5887, https://doi.org/10.1039/C6CP07757A.

58. J. Exner, T. Nazarenus, D. Hanft, J. Kita, and R. Moos, "What Happens during Thermal Post-Treatment of Powder Aerosol Deposited Functional Ceramic Films? Explanations Based on an Experiment-Enhanced Literature Survey," *Advanced Materials* 32, no. 19 (2020): 1908104, https://doi.org/10.1002/adma.201908104.

59. Y. Li, Z. Yuan, D. Li, et al., "Multi-Interface Combination of Bimetallic Selenide and $V_4C_3T_x$ MXene for High-Rate and Ultrastable Sodium Storage Devices," *ACS Nano* 18, no. 6 (2024): 4733–4745, https://doi.org/10.1021/acsnano.3c07977.

60. Y. Li, L. Wang, Z. Sun, et al., "Capacitance-Enhanced Battery: Integrating High-Density Battery Capacity with Supercapacitive Swiftness in an Ultra-Large MXene Architecture," *Advanced Materials* 37, no. 42 (2025): e08336, https://doi.org/10.1002/adma.202508336.

Supporting Information

Additional supporting information can be found online in the Supporting Information section. **Supporting Fig. S1:** Polished Al substrate for being

coated by the PAD process. **Supporting Fig. S2:** Rietveld refinement of powder aerosol deposited NVP/C powders on Al substrate. **Supporting Fig. S3:** Discharge capacities (marked with triangle symbols) and coulombic efficiencies (marked with circle symbols) of 1st set of PAD electrodes in as-deposited (filled symbols) and annealed (unfilled symbols) state. **Supporting Fig. S4:** Discharge curves (cycling at a C-rate of C/10 for 20 cycles between 2 and 4 V at room temperature) of 2nd set of PAD NVP/C electrodes (CAM loading, 9.2 ± 1 mg cm^{-2}); (a) as-deposited, and (b–d) annealed at 250°C, 350°C, 450°C, respectively. **Supporting Table S1:** Refinement structure information of NVP/C CAM. **Supporting Table S2:** Refinement structure information of PAD-NVP cathode film in as deposited state. **Supporting Table S3:** Refinement structure information of PAD-NVP cathode film annealed at 250°C. **Supporting Table S4:** Refinement structure information of PAD-NVP cathode film annealed at 350°C. **Supporting Table S5:** Refinement structure information of PAD-NVP cathode film annealed at 450°C.